mechanism to help interpret these observations in the future.

At low latitudes, some eddies reorganize into elongated east-west currents that are reminiscent of flows on Jupiter and Saturn. The strong variation of the Coriolis effect with latitude in the tropics causes the turbulence there to have a preferred orientation. In some southern deep basins, the Antarctic Circumpolar Current organizes into four persistent filaments maintained by eddy processes, rather than being one broad stream. The currents circling Antarctica are the closest analogs to atmospheric jet streams that can be found in the ocean: they are maintained by similar energy sources related to the latitudinal change of temperature, but their separation scale is much smaller by being tied to the local radius of deformation. These last two situations are ocean realizations of phenomena anticipated from idealized turbulence studies (*32*).

Challenges for the Future

Evidently, much progress has resulted from improving the resolution and hydrodynamical formulations of models. Some comparisons are under way to determine the resolution requirements in different applications, such as climate versus forecast uses, and whether isopycnal coordinates are better than fixed vertical levels. The two methods are probably comparable if the diffusion in leveled models is oriented along isopycnals or if both model grid sizes are well below the local radius of deformation. Hence, future development will probably emphasize improvements of physical components and processes in models, such as the surface mixed layer and sea ice, and outflows and mixing from water-mass formation regions. Furthermore, biogeochemical processes can be included by using methods already tested in coarser grid physical models (*33*).

An immediate goal of modelers is to conduct longer term simulations, including some to full thermodynamic equilibrium. Ocean models will not be fully proven to be well formulated until they can reproduce the equilibrium distributions of temperature, salinity, and other properties as well as the modern spreading of dissolved anthropogenic gases and radioactive tracers. The likelihood that the ocean is capable of different overturning circulations if started from different initial conditions needs to be examined. The natural variability of climate needs to be determined, including the distinct possibility that limits of climate predictability are affected by oceanic turbulence. Finally, a number of past climates and potential future climate (including those influenced by activities of mankind) should be investigated with the aid of high-quality atmospheric models coupled to global ocean models. Most of those efforts require continued growth in computer power.

REFERENCES AND NOTES

1. S. G. Philander, *El Niño, La Nina, and the Southern Oscillation* (Academic Press, San Diego, 1990).
2. S. Manabe and R. J. Stouffer, *Nature* **364**, 215 (1993).
3. F. Nansen, *Oceanography of the North Polar Basin*, vol. 3 of *Science Research* (Christiania, Oslo, Norway, 1902).
4. H. Stommel, *The Gulf Stream: A Physical and Dynamical Description* (Univ. of California, Berkeley, 1965).
5. J. C. Swallow and B. V. Harmon, *Deep-Sea Res.* **6**, 155 (1960).
6. K. Bryan, *J. Comput. Phys.* **4**, 347 (1969).
7. M. D. Cox, in *Numerical Models of Ocean Circulation* (National Academy of Sciences, Washington, DC, 1975), pp. 107–120.
8. H. L. Dantzler, *Deep-Sea Res.* **23**, 783 (1976).
9. W. R. Holland, *J. Phys. Oceanogr.* **8**, 363 (1978).
10. J. C. McWilliams and J. H. Chow, *ibid.* **11**, 921 (1981).
11. A. J. Busalacchi and J. J. O'Brien, *ibid.* **10**, 1929 (1980).
12. M. D. Cox, *ibid.* **15**, 1312 (1985).
13. J. R. Toggweiler, K. Dixon, K. Bryan, *J. Geophys. Res.* **94**, 8217 (1989).
14. A. F. Blumberg and G. L. Mellor, *Three-Dimensional Coastal Ocean Models*, no. 4 (American Geophysical Union, Washington, DC, 1987).
15. D. B. Haidvogel, J. L. Wilkin, R. E. Young, *J. Comput. Phys.* **94**, 151 (1991).
16. R. Bleck and D. B. Boudra, *J. Geophys. Res.* **91**, 7611 (1986).
17. The FRAM Group, *Eos* **72**, 169 (1991).
18. F. O. Bryan, C. W. Böning, W. R. Holland, *J. Phys. Oceanogr.* **25**, 289 (1995).
19. A. J. Semtner and R. M Chervin, *J. Geophys. Res.* **97**, 5493 (1992).
20. G. A. Jacobs *et al.*, *Nature* **370**, 360 (1994).
21. P. D. Killworth, D. Stainforth, D. J. Webb, S. M. Paterson, *J. Phys. Oceanogr.* **21**, 1333 (1991).
22. J. K. Dukowicz and R. D. Smith, *J. Geophys. Res.* **99**, 7991 (1994).
23. A. J. Semtner, in *Proceedings of the 1993 Snowmass Global Change Institute on the Global Carbon Cycle*, T. Wigley, Ed. (Cambridge Univ. Press, Cambridge, in press).
24. R. D. Smith, R. C. Malone, M. Maltrud, A. Semtner, in preparation.
25. R. Bleck, S. Dean, M. O'Keefe, A. Sawdey *Parallel Comput.*, in press.
26. D. Stammer and C. W. Böning, *J. Phys. Oceanogr.* **22**, 732 (1992).
27. W. J. Schmitz and J. D. Thompson, *ibid.* **23**, 1001 (1993)
28. G. Danabasoglu, J. C. McWilliams, P. R. Gent, *Science* **264**, 1123 (1994).
29. V. Zlotnicki, J. McClean, A. J. Semtner, paper presented at the Annual Fall Meeting of the American Geophysical Union, San Francisco, 5 December 1994.
30. S. Ramp, J. McClean, A. J. Semtner, C. A. Collins, K. A. S. Hays, in preparation.
31. D. Stammer, R. T. Tokmakian, A. J. Semtner, C. Wunsch, in preparation.
32. P. B. Rhines, *J. Fluid Mech.* **69**, 417 (1975); R. L. Panetta, *J. Atmos. Sci.* **50**, 2073 (1993).
33. E. Maier-Reimer, *Global Biogeochem. Cycles* **7**, 645 (1993).
34. R. S. Nerem, E. J. Schrama, C. J. Koblinsky, B. D. Beckley, *J. Geophys. Res.* **99**, 24565 (1994).

35. The most recent modeling efforts discussed here are funded by the Department of Energy's Office of Health and Environmental Research under CHAMMP (Computer Hardware, Advanced Mathematics, Model Physics) and by the National Science Foundation's Physical Oceanography Program under WOCE. The TOPEX satellite data was provided by Caltech's Jet Propulsion Laboratory and the Goddard Space Flight Center through the support of the National Aeronautics and Space Administration. The computational resources for the simulations shown in the figures were provided by the National Center for Atmospheric Research, Los Alamos National Laboratory, and the Pittsburgh Supercomputing Center.

Numerical Models of Caldera-Scale Volcanic Eruptions on Earth, Venus, and Mars

Susan Werner Kieffer

Volcanic eruptions of gassy magmas on Earth, Venus, and Mars produce plumes with markedly different fluid dynamics regimes. In large part the differences are caused by the differing atmospheric pressures and ratios of volcanic vent pressure to atmospheric pressure. For each of these planets, numerical simulations of an eruption of magma containing 4 weight percent gas were run on a workstation. On Venus the simulated eruption of a pressure-balanced plume formed a dense fountain over the vent and continuous pyroclastic flows. On Earth and Mars, simulated pressure-balanced plumes produced ash columns, ash falls, and possible small pyroclastic flows. An overpressured plume, illustrated for Mars, exhibited a complex supersonic velocity structure and internal shocks.

Calderas are large craters formed by the collapse of the summits of volcanoes after eruptions of tens of cubic kilometers or more of magma (Fig. 1A). A large caldera eruption, with mass fluxes believed to be $>10^8$ kg/s, has never been witnessed on Earth. Such "caldera-scale" eruptions can produce plumes that reach the stratosphere as well as ash flows (so-called ignimbrite

The author is in the Department of Geological Sciences, University of British Columbia, Vancouver, British Columbia V7W 2H9, Canada.

sheets) that cover thousands of square kilometers. A well-known example is the Valles caldera and its deposits that cover most of northern New Mexico (Fig. 1A).

Calderas have been observed on other planetary bodies such as Mars (Fig. 1B) and Venus. Indeed, on Io, a moon of Jupiter, the Voyager spacecraft showed that calderas occur as landforms and that caldera-scale eruptions are occurring at the present time. Observations of these planetary analogs can provide us with a rich database for comparison and contrast of the processes inferred for Earth. Why do some of the volcanic landforms look so similar to our terrestrial ones, and why do some look so different (Fig. 1, A through C)? The present study sought to understand the relation between eruption dynamics and global parameters (such as gravity and atmospheric pressure and temperature) and to compare and contrast the dynamics of eruption on the different planets.

Visualization of the fluid dynamics of caldera-scale eruptions is difficult because the flow fields are extremely complex: They are unsteady, three-dimensional, and multicomponent. The small eruption plume of Mount St. Helens (Fig. 1D) offers some insights about volcanic plumes in general. The initial unsteady-state development of the plume can be inferred from a few turbulent cells far downwind. The steady-state configuration of the plume (its height and shape) is visible at the mountain summit on the upwind side. Segregation of the multicomponent flow is evidenced by ash falling out from the plume and leaving a steam-enriched column (white). A dense ground-level flow is moving down the slope to the right, and ash separating from the higher plume is drifting downward to feed the ground-hugging flow. These are complex and generally nonlinear processes that cannot be scaled for study under controlled laboratory conditions.

The numerical modeling of eruptions is revolutionizing theoretical volcanology because it allows the study of many aspects of these eruptions by direct solution of the Navier-Stokes equations. These techniques were first introduced and applied to examine the conditions of generation of ash columns and pyroclastic flows (*1–5*). The philosophy adopted by these authors was to define processes during different phases of eruptions in order to provide a general fluid-dynamic framework for interpretation of volcanic deposits in the field. Another group has developed a similar set of models for a smaller type of eruptions—those of Mount Vesuvius, Italy (*6–9*). This group is attempting to predict volcanic hazards, especially in the heavily populated Mount Vesuvius area, by using the numerical models as a basis for formulating a risk assessment methodology. Such models can guide field observations, and in turn there is an ongoing need for more observations and for more ways to test the simulations. Planetary observations can serve several purposes here: The models can guide interpretations of remote sensing data, and the data in turn serve as a new nonterrestrial database for constraining the models. At the present time, the terrestrial models referenced above have not been extended to other planets. Instead, parametric models and steady-flow approximations have been adopted in an attempt to understand complex volcanic plumbing systems, eruption parameters, and geologic and geomorphic effects that exist on other planets (*10–17*).

Going beyond the parametric models is conceptually and computationally difficult because planetary volcanism occurs in a wide variety of geologic and atmospheric conditions (Table 1). Atmospheric temperature and gravity vary by an order of magnitude from one planet to another, but atmospheric pressure varies by 14 orders of magnitude. It is not feasible to investigate the effect of individual parameters systematically one by one, because an inordinate amount of computational time would be required. Therefore, I chose to examine how the fluid dynamics of a relatively gas-rich eruption on Earth would change if this

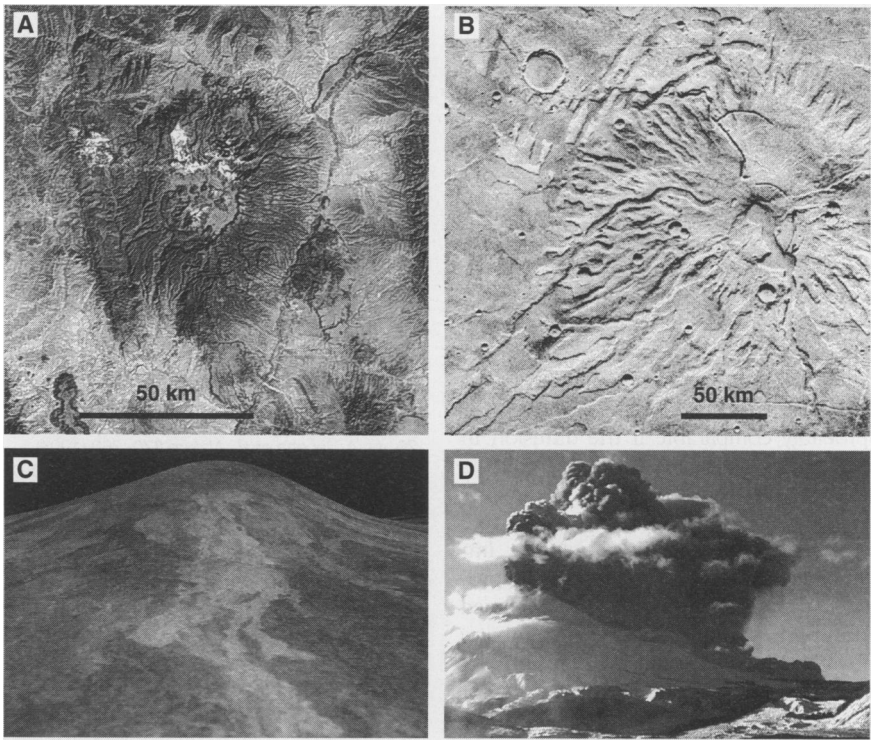

Fig. 1. (**A**) The Valles caldera on Earth, as viewed from Landsat. The caldera diameter (center) is about 20 km. (**B**) NASA Viking spacecraft image of Tyrrhena Patera on Mars. This structure is believed to be hydromagmatic in origin and to have formed early in martian history, when water was more abundant than at present (*31*). Note the gullies and erosional remnants on the lower flanks. (**C**) NASA Magellan spacecraft perspective image of the large volcanic structure Sif Mons on Venus. The flows in the foreground are 3 to 8 km in width; see (*27*). (**D**) Eruption of Mount St. Helens in March 1980. The plume is about 1 km above the summit. [Photo by S. W. Kieffer]

Table 1. Planetary parameters: g, acceleration due to gravity; T, atmospheric temperature at the surface; P, atmospheric pressure at the surface; and X, typical atmospheric and volcanic gas composition. Properties of Io and Triton are included for completeness; however, because of their unique planetary histories as well as computational complexity at extremely low temperatures and low pressures, the results for Triton and Io are not included in the text.

Planet	g (cm/s^2)	T (K)	P (bar)	X
Earth*	980	300	1.0	H_2O, CO_2, N_2
Venus†	860	700	70 to 100‡	CO_2, H_2O, SO_2
Mars*	380	273	6×10^{-3} to 8×10^{-3}§	CO_2, H_2O
Triton	90	38	16×10^{-6}	N_2, CH_4
Io	180	130	10^{-7} to 10^{-12}	SO_2, S

*H_2O used in model. †CO_2 used in model. ‡70 bar used in model. §6×10^{-3} bar used in model.

eruption occurred on Venus, which has a high-pressure and high-temperature atmosphere, and on Mars, which has a low-pressure and low-temperature atmosphere. The scale chosen is typical of large stratovolcano to small caldera eruptions on Earth (vent radius of 200 m, mass fluxes of 10^6 to 10^{10} kg/s, and distance scales of tens of kilometers). The mass flux and dimensions of the plinian phase of the 18 May 1980 Mount St. Helens eruption are now thought to have been within this range (conduit diameter of tens of meters, smaller than that considered here; mass flux of $\sim 10^7$ kg/s; water content of about 4 weight %; and exit velocities of several hundred meters per second) (9).

Although spectacular active volcanism occurs on Io and low-temperature geyser-like plumes are observed on Triton, a moon of Neptune, these planetary bodies have such grossly different histories from those of Earth, Venus, and Mars that they are not considered further. The focus here is on the three planets that have had somewhat similar origins and evolutions and therefore plausibly have magmas of similar compositions and volatile contents.

Planetary Parameters

From fluid dynamics of aeronautical nozzles (*18*), we know that large variations in pressure have a major influence on the fluid flow behavior and that atmospheric temperature, gravity, and gas composition have only a secondary effect. Modeling the flow from a high-pressure to a low-pressure condition is difficult if the pressure ratio is greater than about 10 because the flow fields are nonlinear and contain traveling and standing waves. The equations are not analytically solvable and they can be numerically unstable wherever pressure gradients are steep.

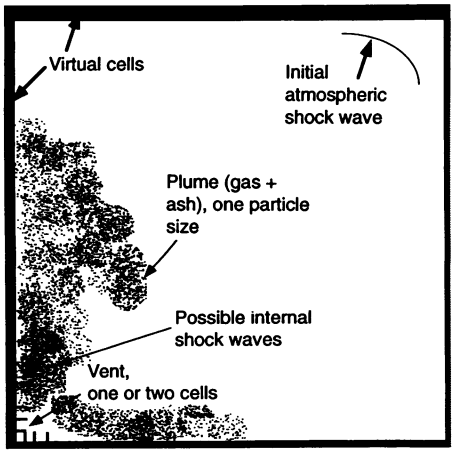

Fig. 2. Schematic of the computational domain. Each boundary hides one cell (the virtual cells), so the true grid size is equal to the number of visible cells in each direction plus 2.

The ratio of vent pressure to atmospheric pressure is the most important parameter to be specified. However, even at small terrestrial eruptions volcanic vent pressures cannot be measured directly; indeed, this is a difficult measurement even in a geyser. It is likely that the vent pressure varies with time as an eruption evolves (9). For modeling purposes, two different extremes were examined in the literature. In one set of models, vent pressure is assumed to be equal to atmospheric pressure; this is the so-called pressure-balanced condition (*11*, *15*, *16*). This assumption permits many mathematical simplifications that allow analytic or semianalytic solutions applicable to planetary problems. However, fulfillment of the pressure-balanced condition requires special conditions of vent friction and geometry (*19*). These conditions may not be obtained early in eruptions before a vent is cleared, or in short eruptions [for example, the lateral blast at Mount St. Helens (*20*)], or on planets with low atmospheric pressure (*14*). Therefore, a second set of models that allow for higher pressure at the vent has been developed. For example, overpressuring by factors of 2 to 150 has been examined for terrestrial eruptions (*3*, *14*, *20*). These assumptions are compared and contrasted in the calculations for Mars below.

Approach

The calculations presented are for central vent eruptions. Caldera eruptions are, in fact, usually more complex than this: The eruptions may start at a central vent, but as magma is withdrawn and the volcanic summit starts to collapse, the eruptions may evolve along arcuate fissures bounding the caldera. Therefore, a central vent eruption is the simplest, but not necessarily only, geometry that could be chosen. Only eruption simulations with flat terrain are shown, but the effects of topography, such as an annular rim surrounding the central vent, can be substantial (*5*). A rim can deflect flows back in toward the vent or can totally confine flows within the caldera. Several simulations of the effect of the rim were run for Venus and Mars, and the effects were generally as reported in (*5*).

I used the approach of Wohletz, Valentine, and colleagues (*1*, *3*, *5*, *21*, *22*), which is based on explicit numerical solutions of the equations of conservation of mass, momentum, and energy (*23*). A fluid is assumed to erupt from a cylindrically symmetric vent (Fig. 2). The erupting fluid is a two-component mixture of gas and dispersed ash particles. The gas is described by the ideal gas equation of state and the ash particles are assumed to be incompressible. The conservation equations are applied to the ash and gas components separately, so that they may have different temperatures and velocities. The components interact with each other through drag forces and heat transfer. The governing equations of motion and constitutive relations form a system of eight partial differential equations and eight algebraic equations with 16 dependent variables [given in (*21*)]. The equations are approximated by finite difference methods (*24*) and are solved on large supercomputers or standard workstations, depending on problem size.

In the calculations, ash and gas enter the computational domain through a vent (Fig.

Table 2. Other parameters used in the computer simulations (γ, isentropic exponent; ρ, density; c, heat capacity; and K, kelvin). The drag coefficient c_d was 1.0 in all simulations. The kinematic viscosity was taken to be representative of the averaged pressure and temperature conditions on the planets, and therefore varies considerably. The viscosity coefficient q_0 was 0.1 in all runs for which the cell size was 200 m (*2*), giving a mixing length of about 20 m.

Parameter	Earth	Venus	Mars: Pressure-balanced	Mars: Overpressured
γ, gas phase	1.33	1.18	1.3	1.3
Vent pressure (bar)	1.0	70	0.006	1.0
Void fraction gas (%)	99.8	72.4	99.9	99.8
Mass flux at vent (kg s^{-1})	1.8×10^8	2.1×10^{10}	1.1×10^6	1.8×10^8
Mach number	2.0	3.0	2.0	2.0
ρ_{atm}, base (g cm^{-3})	7.88×10^{-4}	5.43×10^{-2}	5.20×10^{-6}	5.20×10^{-6}
ρ_{gas} (g cm^{-3}) at 1200 K	1.99×10^{-4}	3.2×10^{-2}	1.18×10^{-6}	1.97×10^{-4}
Internal energy, gas (ergs g^{-1})	1.68×10^{10}	1.26×10^{10}	1.69×10^{10}	1.69×10^{10}
ρ_{plume}, inflow (g cm^{-1})	4.93×10^{-3}	5.74×10^{-1}	2.96×10^{-5}	4.91×10^{-3}
c_{solid} (ergs g^{-1} K^{-1})	9.5×10^6	9.5×10^6	9.5×10^6	9.5×10^6
c_{gas} (ergs g^{-1} K^{-1})	1.41×10^7	1.05×10^7	1.41×10^7	1.41×10^7
Gas conductivity (ergs g^{-1} s^{-1} K^{-1})	5.0×10^3	5.88×10^3	5.0×10^3	5.0×10^3
Kinematic gas viscosity (cm^2 s^{-1})	1.3	9×10^{-3}	211	1.3

2) beginning at time $t = 0$. The proportions of ash and gas are specified, as are the initial velocity, temperature, and pressure. These components flow into an atmosphere that has the same composition as the gas phase in the erupting fluid but may have a different temperature. The atmosphere is initially isothermal and its pressure and density decrease exponentially with height.

Because the geometry is cylindrically symmetric, the calculations are only performed for a half-space. The symmetry axis is defined as a reflecting boundary. The top and right-hand boundaries are outflow boundaries. The bottom boundary is treated as a frictionless substrate [see (5)]. Practical limitations require a mesh size of 100 to 200 m and domain sizes of no more than 150 by 150 cells; hence, these calculations are for large-scale, not outcrop-scale, phenomena.

Initial Conditions and Fluid Properties

For even the simplest solutions, many parameters are required to describe the initial and boundary conditions (atmospheric conditions, gravity, and fluid composition) (Table 1) and fluid properties (vent conditions, heat capacities, and thermal and mechanical interaction parameters) (Table 2). A systematic study of the variation of each of these parameters would be prohibitively time-consuming. Therefore, I studied one specific type of caldera-scale eruption and included as many specific global parameters as possible in each simulation.

The reference case is for a magma that contains 4 weight % gas. This is similar but not identical to cases of plinian eruptions with 1.7 weight % gas that have been well studied numerically (*3*, *5*, *21*, *22*) and in the field (*2*, *25*). The increase in gas content was required for extrapolation to the higher atmospheric pressure conditions of Venus. A volume fraction of 70 weight % is usually taken as the criterion for magma fragmentation and production of a dusty gas plume (*13*); if the gas content is only 1.7 weight %, the volume fraction on Venus would only be 50 weight %, which is an unreasonably low volume fraction for this type of modeling. A CO_2 content of 4 weight % produces a void fraction of 72 weight % at 70-bar pressure on Venus, and so 4 weight % was chosen as the gas content for all simulations.

For the simulations on Earth and Mars, the gas phase was assumed to be H_2O so that 1-bar vent conditions on both planets could be directly compared. Although gas composition is included as a parameter in the simulations, the composition has relatively little influence on the results compared with other factors discussed here. In particular, for plumes that are as heavily laden with ash particles as these, the expansion of the gas is more strongly controlled by heat transfer from the particles to the gas than by the composition of the gas itself. For all simulations, the temperature of the gas and ash exiting the vent was assumed to be 1200 K, the ash particle radius was 0.01 cm, and the material density of the particles was 2000 kg/m^3. In the simulations, vent pressure was taken as either atmospheric (Venus, 70 bar; Earth, 1 bar; Mars, 0.006 bar) or greater than atmospheric. For the overpressured case on Mars, the pressure at the vent was taken to be 1 bar, that is, the vent conditions matched the assumed terrestrial vent conditions.

A number of parameters could be held constant in the simulations, such as vent radius, vent velocity, vent Mach number, mass flux, volume fraction volatiles, vent pressure, and temperature. In the simulations for all three planets, I chose to hold the vent radius at 200 m, and the initial vent velocity, v, constant at 290 m/s. These values produce different exit Mach numbers (v/a, where a is the mixture sound speed) on the three different planets because the sound speed of the erupting mixture changes with vent pressure and particle loading. On Earth and Mars, where the particle loading is relatively light and the mixture is homogeneous, sound speeds are similar (145 m/s) and therefore so are the Mach numbers (2.0). On Venus, the higher vent pressure of 70 bar causes higher particle concentrations, which reduces the sound speed to 93 m/s; the Mach number correspondingly increases to 3.0.

Mass flux is often taken as one of the controlling parameters in volcanic plume dynamics (*15*). However, another consequence of holding vent radius and velocity constant is that mass flux is not the same in all of the simulations (Table 2), which directly reflects the effect of vent pressure on the mixture density and mass flux at the vent. The mass flux is the same in two of the simulations, the terrestrial and overpressured martian eruptions; thus, examination of these two cases enables a direct comparison of the other parameters on the eruption dynamics.

Fluid Dynamics in the Simulations

The large-scale behavior of a volcanic eruption column is determined by the relative values of four different types of forces (*1*, *2*): inertia, pressure gradients, interphase drag, and gravitation. In the following, a plume comprises any of the gas and ash material above the vent, and a column is the main vertical part of the eruption flow field above the vent. When a column develops with sustained upward movement, it is referred to by volcanologists as a plinian column (Fig. 1A), and I adopt that term loosely to interpret the simulations. A column that collapses back upon itself and forms a downward-moving sheath is referred to as a fountain, and the place where it reimpacts the ground is the stagnation point or reimpact zone. Laterally moving, ground-hugging flows that result from the fountain collapse are called pyroclastic flows. A column that attains neutral buoyancy is one that stagnates in

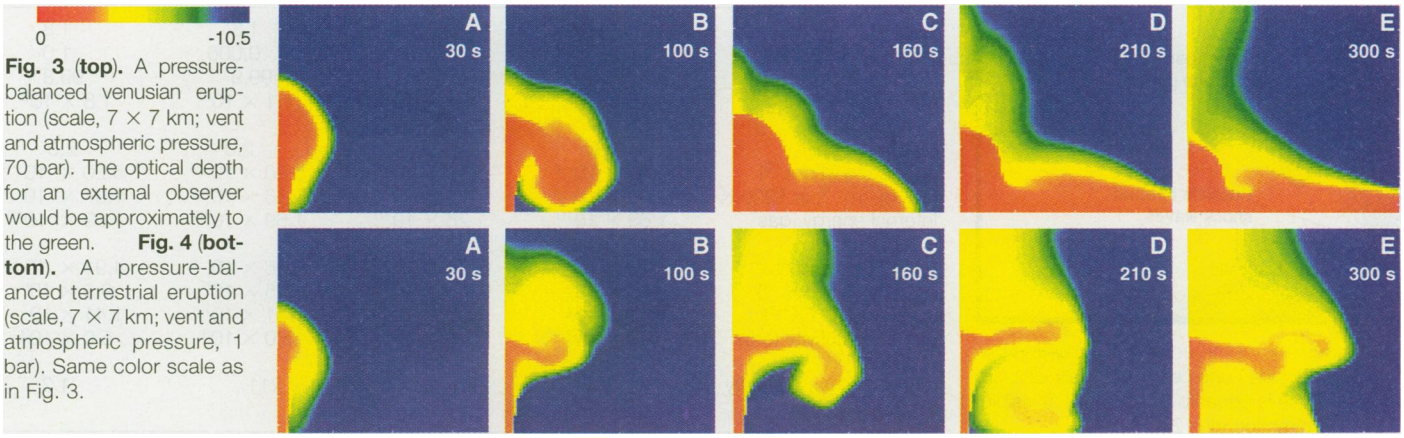

Fig. 3 (top). A pressure-balanced venusian eruption (scale, 7 × 7 km; vent and atmospheric pressure, 70 bar). The optical depth for an external observer would be approximately to the green. **Fig. 4 (bottom).** A pressure-balanced terrestrial eruption (scale, 7 × 7 km; vent and atmospheric pressure, 1 bar). Same color scale as in Fig. 3.

its ascent but does not collapse to form a fountain (this is a rather special definition of the term but is convenient for the following discussion). The working surface is the unsteady flow at the top of the column where large-scale vorticity and entrainment yield an increased diameter as the column penetrates into the atmosphere. In the computer-generated color images of different time points in the simulated eruptions (Figs. 3 through 6), the parameter plotted is the logarithm of the volume fraction of solid particles, represented by a color scale.

Venus. The initial pressure chosen for the simulated Venus eruption was 70 bar, in balance with the venusian atmosphere. The erupting material is therefore substantially denser than that of the terrestrial jet (note the different shades of red in the core regions of Figs. 3 and 4). The jet erupts from the vent to an altitude of about 4 km and then collapses back to form a low fountain. This fountain feeds pyroclastic flows that run radially outward from the impact point of the collapsing fountain. In addition, some of the erupted material moves back radially inward from the impact point to recirculate back into the rising fountain.

An interesting wave develops within the pyroclastic flow about 2 km radially from the vent (Fig. 3, C through E). This wave has many characteristics of a standing hydraulic jump. Because of the assumed cylindrical geometry, the wave is analogous to the circular hydraulic jump that can be produced in a kitchen-sink experiment by holding a flat plate under a downward spout of water. Under most kitchen conditions, fluid spreads radially from the impinging jet toward the edge of the plate in two distinct flow regimes. Near the impingement point, the flow is shallow and fast as it spreads radially, a supercritical flow regime. Toward the edge of the plate, the flow becomes deep and slow, a subcritical flow regime. These two regimes are separated by a standing circular wave, a hydraulic jump. Further study of the development and properties of these waves in multiphase fluids should yield an understanding of the nonlinear dynamics inherent in these complex systems. The high pressure of the venusian atmosphere suppresses the immediate formation of a dusty plume rising vertically over the fountain (compare Fig. 3 with Fig. 4). In fountain-forming eruptions of dense material like this, the primary way that material is lofted to high elevations above the main fountain is by mixing of the high-density plume with the lower density atmosphere. However, in this case, the formation of the hydraulic jump and its interaction with the main column gives rise to an elutriated ash cloud that eventually rises above the low fountain (Fig. 3, C through E). This evolution of the simulated eruption on Venus resembles in most ways the well-documented plinian conditions for terrestrial jets with 1.7 weight % water (*3*). However, the properties of the simulated terrestrial eruption with 4 weight % water are very different from those of this venusian jet or of a terrestrial eruption with 1.7 weight % water.

Earth. The relatively gassy initial condition of 4 weight % water produces a terrestrial plume that is almost balanced between conditions that form towering plinian gas and ash columns and those that produce low fountains and dense pyroclastic flows. Although the parameters cannot be quantified for a real and complex volcanic situation, the balance between plinian column conditions and fountain conditions is influenced by the thermogravitational parameter, the Rouse number, the Richardson number, particle terminal velocities, the pressure ratio between the vent fluid and the atmosphere, the density ratio between the vent fluid and the atmosphere, and the initial Mach number (*3*, *5*, *7*, *21*). I describe this jet as having attained a height of neutral buoyancy.

Initially, the plume rises from the vent and develops a working surface at the top as a result of the entrainment of the atmosphere (Fig. 4, A and B). However, upon reaching an altitude of ~4 km, the working surface and the denser core of the plume stall. Some material falls back toward the ground (Fig. 4, C and D) and the column begins to evolve into a classic low fountain that feeds outward and inward flows (Fig. 4, B through D; compare with Fig. 3, B through D). However, the flow conditions are poised at the balance between those of a rising column and of a collapsing column; the fountain does not become well developed, and the pyroclastic flows are only weakly fed (Fig. 4E). The stagnant cap of the plume at the neutral buoyancy altitude of about 3 km feeds the ash falls, the rising plinian column, and, only intermittently, the ash flows. The eruption column consists of a complex field of rising and falling material, perhaps in an oscillating manner (*9*).

Several of these later features in these computer simulations are also visible in the photograph of the small Mount St. Helens eruption (Fig. 1D). The dense column rising above the vent of Mount St. Helens is equivalent to the plinian column rising above the vent in the computer simulation; the fortuitous wind direction makes the Mount St. Helens column resemble the half-space of the simulation. The formation of the white steam-enriched cap above the Mount St. Helens plume by the separation of the multiphase solid and gas (water vapor) components is equivalent to the separation of the ash-enriched (orange) and vapor-enriched (yellow and green) components of the simulated plume. The coalescence of the downward-falling ash into a pyroclastic flow at Mount St. Helens is equivalent to the falling ash and ground-hugging pyroclastic flow in the simulation.

Mars. The evolution of the pressure-balanced martian simulation mimics that of the pressure-balanced terrestrial simula-

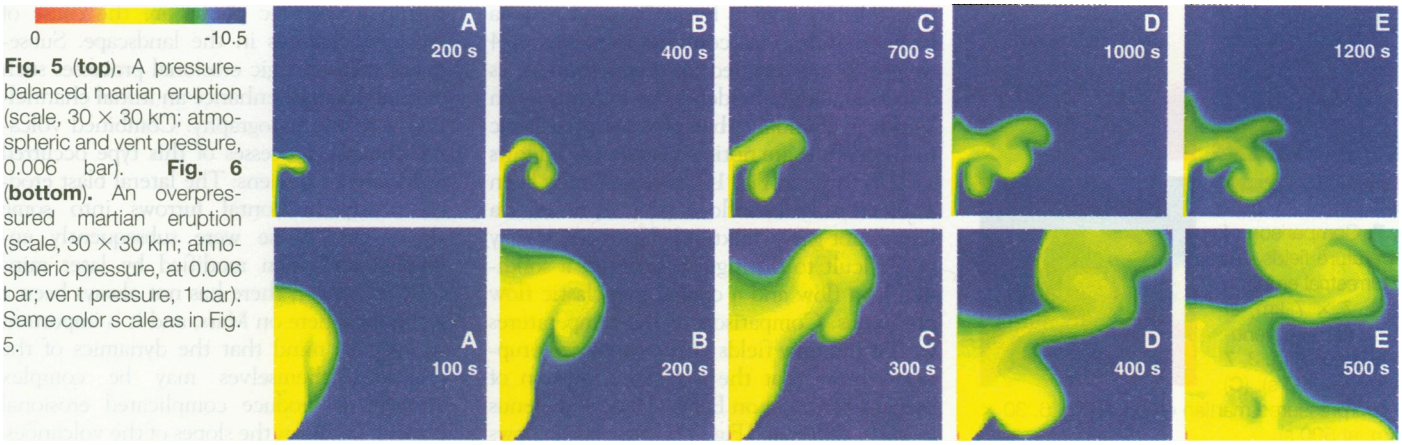

Fig. 5 (top). A pressure-balanced martian eruption (scale, 30 × 30 km; atmospheric and vent pressure, 0.006 bar). **Fig. 6 (bottom).** An overpressured martian eruption (scale, 30 × 30 km; atmospheric pressure, at 0.006 bar; vent pressure, 1 bar). Same color scale as in Fig. 5.

tion (Fig. 5, A through E), even though there is a 166-fold difference in absolute pressures. The general yellow and green hues in the martian simulation reflect the much lower density of the plume. The distance scale of the affected area on Mars is much larger than on Earth (tens of kilometers in each direction rather than a few kilometers). The times to reach equivalent column configurations are correspondingly longer, on the order of 1000 seconds instead of a few hundred seconds. The plume reaches a height of neutral buoyancy and ash rises or falls only intermittently and slowly (Fig. 5, C through E).

In contrast, the simulation of the overpressured martian eruption exhibits a fascinating array of supersonic flow features near the vent and out to a distance of approximately 10 km (Fig. 6, A through E). The first fluid out of the vent mixes with the atmosphere and forms a large working surface that reaches an altitude of 20 km within 100 s (Fig. 6A). This working surface appears to break off and rise above 30 km (Fig. 6, B and C). Detailed analysis of this breakup is not warranted because the viscosity and entrainment assumptions in the simulation are so simplified that they may cause artifices in the behavior of the working surface at long simulation times.

Near the vent, the column emerges in the typical configuration of a supersonic jet (*20*). The rapid change of color from the deep red of vent conditions of 1 bar to the lighter colors illustrates how rapidly the gas decompresses. Fluid accelerates outward in all directions from the vent, covering a much larger near-vent area than does the pressure-balanced jet (compare the red zones in Figs. 5B and 6B to see vent size and supersonic spreading). The fluid emerges from the vent and accelerates to about 7 km where it forms a shock wave, the so-called Mach disk shock in aeronautics. The slight color inflection at an altitude of ~7 km shows the position of this shock. Lateral oblique shocks (not readily visible in the plots shown) determine the shape of the jet. [A relatively common terrestrial analog can be seen in the shape of supersonic plumes above many geothermal wells (*26*)].

This near-vent flow pattern is identical to that proposed for supersonic flow out of the vent during the lateral blast at Mount St. Helens, 18 May 1980 (*20*). The large pressure gradients between the vent and the atmosphere produce accelerations that are large compared to gravitational accelerations. As a result, material is thrown much farther from the vent than under pressure-balanced conditions. After material passes through the shock waves, it decelerates and gravitational forces become important. Some of the fluid falls back to the ground, reimpacting at a distance of ~10 km. From this reimpact zone, material forms a ground-hugging pyroclastic flow. A supersonic jet of this type develops a broad umbrella that covers a much larger area and generates substantial high-velocity activity at distances many vent diameters from the main eruption.

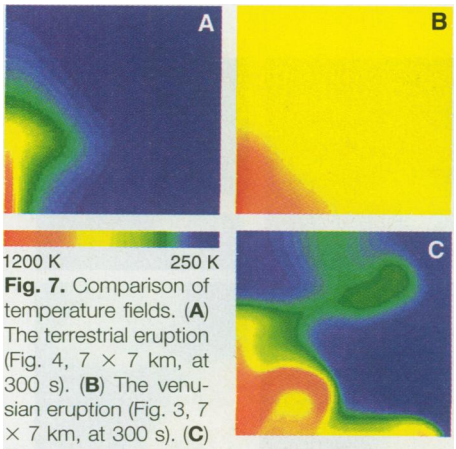

Fig. 7. Comparison of temperature fields. (**A**) The terrestrial eruption (Fig. 4, 7 × 7 km, at 300 s). (**B**) The venusian eruption (Fig. 3, 7 × 7 km, at 300 s). (**C**) The overpressured martian eruption (Fig. 6, 30 × 30 km, at 500 s).

Planetary Interpretations

Numerical simulations provide a rich resource for learning about nonlinear fluid dynamic processes because powerful computers can now solve relatively complex systems of equations, and because visualization tools are excellent. The influence of the variation of global planetary parameters on volcanic eruption dynamics, including the shape, extent, and internal structure of complex plumes, has been illustrated in the simulations presented here.

As an example of how the consideration of the fluid-dynamic structure of plumes may influence our interpretation of photographs of features on the planets, consider the flows on Venus (Fig. 1C) and the gullied flanks of the volcano on Mars (Fig. 1B). There has been considerable controversy about whether pyroclastic volcanism can occur on Venus because the high atmospheric surface pressure inhibits bubble formation and magma fragmentation. Gas contents in excess of 4 weight % are required for fragmentation, as discussed above. Evidence for volcanism on Venus is abundant, but obvious pyroclastic (ash) deposits are noticeably rare (*27*). Flows such as those in Fig. 1C have generally been assumed to be lava flows (that is, flows of a liquid, not gassy, mixture). However, it may be difficult to distinguish between a solidified lava flow and a cooled pyroclastic flow on Venus. Comparison of the temperatures within the flow fields of the simulated eruptions shows that the thermal evolution of pyroclastic ejecta on Earth, Mars, and Venus is quite different (Fig. 7). Pyroclastic flows on Venus are much hotter than those on Earth for much longer distances and, presumably, for much longer times because they are entraining a much hotter atmosphere (700 K) than such flows on Earth or Mars. The temperatures are high enough that substantial welding of the ash particles may occur as the flows slow down and the ash particles come in contact with each other. Thus the material, which was initially a dispersed mixture of gas and ash when it left the vent, evolves to a liquid-like state. In this state, it can even continue flowing as if it were a liquid lava, and it may ultimately come to rest with geomorphic features reflecting its secondary liquid-like state rather than its initial ash and gas state (a process called rheomorphism). Because of this complexity, pyroclastic deposits around calderas may be difficult to recognize on Venus.

For a second example of how knowledge of the fluid-dynamic structure of a plume might influence interpretation of features on a volcano, consider the striking sinuous channels visible on the lower flanks of such calderas as Hecates Tholus or Tyrrhena Patera (Fig. 1B). These channels typically start tens of kilometers downslope from the summit calderas. They have been variously interpreted as originating from volcanic density currents (*28*) or as fluvial channels (*29*). Our conventional terrestrial-based understanding of plumes as tall but relatively narrow plinian columns would predict that channels resulting from volcanic density currents should start relatively high on the slopes because the reimpact zones are relatively close to the summits in terrestrial plinian eruptions. However, the simulation of the overpressured jet on Mars (Fig. 6) suggests a fluid-dynamic reason that the gullies may start so far down the slopes: An overpressured eruption blasts material out to 10 km or more, where it falls back to a reimpact zone. The reimpact zone is at much greater distances from the vent than on Earth or Venus. The pyroclastic flows emanating from this zone have high velocities and could cause the distal gullying observed. In this case, the initial fluid-dynamic conditions within a volcanic plume are the cause of erosional features in the landscape. Subsequent meteorologic erosional processes such as rainfall might enhance an initial channelized volcanic topography. Combined volcanic-climatic processes of this type occurred at Mount St. Helens: The lateral blast eroded nearly horizontal furrows into some slopes, and these were subsequently enhanced and then modified by later rains (*30*). However, there has not always been a wet atmosphere on Mars, and it is important to keep in mind that the dynamics of the eruptions themselves may be complex enough to produce complicated erosional features far down the slopes of the volcanoes.

Conclusions

Many processes need to be considered in interpretations of terrestrial and planetary landforms. Until the advent of modern computers, complex internal fluid-dynamic processes such as those illustrated here could not be easily considered because the highly nonlinear processes are not susceptible to analytic or semianalytic analyses. The use of numerical simulations to solve and visualize fluid-dynamic processes and constraints can be combined with laboratory and field observations to enhance our understanding of complex geologic phenomena on Earth and on the other planets.

REFERENCES AND NOTES

1. K. H. Wohletz, T. R. McGetchin, M. T. Sanford II, E. M. Jones, *J. Geophys. Res.* **89**, 8269 (1984).
2. G. A. Valentine, thesis, University of California, Santa Barbara (1988); also as *Field and Theoretical Aspects of Explosive Volcanic Transport Processes* (Los Alamos Natl. Lab. Rep. LA-11441-T, UC-702, 1988).
3. G. A. Valentine and K. H. Wohletz, *J. Geophys. Res.* **94**, 1867 (1989).
4. _____, *Geology* **7**, 641 (1989).
5. _____, S. W. Kieffer, *Geol. Soc. Am. Bull.* **104**, 154 (1992).
6. F. Dobran, Ed., *Prospects for the Simulation of Volcanic Eruptions* (Giardini, Pisa, Italy, 1991); *J. Volcanol. Geotherm. Res.* **49**, 285 (1992).
7. _____, A. Neri, G. Macedonio, *J. Geophys. Res.* **98**, 4231 (1993).
8. F. Dobran, A. Neri, M. Todesco, *Nature* **367**, 551 (1994); G. Macedonio, F. Dobran, A. Neri, *Earth Planet. Sci. Lett.* **121**, 137 (1993).
9. P. Papale and F. Dobran, *J. Geophys. Res.* **99**, 4355 (1994).
10. L. Wilson, *Geophys. J. R. Astron. Soc.* **30**, 381 (1972); *ibid.* **45**, 543 (1976).
11. _____, R. Sparks, T. C. Huang, N. Watkins, *J. Geophys. Res.* **83**, 1829 (1978); L. Wilson, *J. Volcanol. Geotherm. Res.* **8**, 297 (1980).
12. L. Wilson and J. W. Head III, *J. Geophys. Res.* **86**, 2971 (1981).
13. J. W. Head III and L. Wilson, *ibid.* **91**, 9407 (1986).
14. S. W. Kieffer, in *Explosive Volcanism: Inception, Evolution, and Hazards* (National Academy Press, Washington, DC, 1984), p. 143.
15. L. Wilson, H. Pinkerton, R. MacDonald, *Annu. Rev. Earth Planet. Sci.* **15**, 73 (1987).
16. L. Wilson and G. P. L. Walker, *Geophys. J. R. Astron. Soc.* **89**, 657 (1987).
17. J. W. Head and L. Wilson, *J. Geophys. Res.* **97**, 3877 (1992).
18. P. A. Thompson, *Compressible-Fluid Dynamics* (McGraw-Hill, New York, 1972).
19. L. Wilson, *Geophys. J. R. Astron. Soc.* **63**, 117 (1980).
20. S. W. Kieffer, *U.S. Geol. Surv. Prof. Pap. 1250*, (1981), p. 379.
21. K. H. Wohletz and G. A. Valentine, in *Magma Storage and Transport*, M. Ryan, Ed. (Wiley, New York, 1990).
22. G. A. Valentine, K. H. Wohletz, S. W. Kieffer, *J. Geophys. Res.* **96**, 21887 (1991).
23. F. H. Harlow and A. A. Amsden, *J. Comput. Phys.* **17**, 19 (1975).
24. DASH is a computer code developed at Los Alamos National Laboratory to study dusty air shocks. The simulations reported here took several to a dozen hours on an SGI Indigo II workstation.
25. G. Valentine, *Bull. Volcanol.* **49**, 616 (1987).
26. S. W. Kieffer, *Rev. Geophys.* **27**, 3 (1989).
27. J. W. Head *et al.*, *Science* **252**, 276 (1991).
28. C. E. Reimers and P. D. Komar, *Icarus* **39**, 88 (1979).
29. P. J. Mouginis-Mark, L. Wilson, J. W. Head III, *J. Geophys. Res.* **87**, 9890 (1982).
30. S. W. Kieffer and B. Sturtevant, *ibid.* **93**, 14793 (1988).
31. R. Greeley and D. A. Crown, *ibid.* **95**, 7133 (1990).

32. Supported by NASA grants NAGW-1740 (at Arizona State University) and 5-56791 (at the University of British Columbia). Related preliminary work on DASH was supported by Los Alamos National Laboratory Institute of Geophysics and Planetary Physics. I was greatly assisted in various stages of this project by A. Levine, T. Morino, M. Morrissey, M.-L. Woo, and G. Yuan. Special thanks are due to G. Valentine and K. Wohletz for continued wisdom on DASH.